PHYSICAL REVIEW B **108**, 205417 (2023)

Quantum dot source-drain transport response at microwave frequencies

Harald Havir,[1,*] Subhomoy Haldar,[1] Waqar Khan,[1] Sebastian Lehmann,[1] Kimberly A. Dick,[1,2] Claes Thelander,[1]
Peter Samuelsson,[3] and Ville F. Maisi[1]
[1]*NanoLund and Solid State Physics, Lund University, Box 118, 22100 Lund, Sweden*
[2]*Center for Analysis and Synthesis, Lund University, Box 124, 22100 Lund, Sweden*
[3]*Physics Department and NanoLund, Lund University, Box 118, 22100 Lund, Sweden*

(Received 23 March 2023; revised 12 October 2023; accepted 16 October 2023; published 16 November 2023)

Quantum dots are frequently used as charge-sensitive devices in low-temperature experiments to probe electric charge in mesoscopic conductors where the current running through the quantum dot is modulated by the nearby charge environment. Recent experiments have operated these detectors using reflectometry measurements up to gigahertz frequencies rather than probing the low-frequency current through the dot. In this work, we use an on-chip coplanar waveguide resonator to measure the source-drain transport response of two quantum dots at a frequency of 6 GHz, further increasing the bandwidth limit for charge detection. Similar to that in the low-frequency domain, the response is here predominantly dissipative. For large tunnel coupling, the response is still governed by the low-frequency conductance, in line with Landauer-Büttiker theory. For smaller couplings, our devices showcase two regimes where the high-frequency response deviates from the low-frequency limit and Landauer-Büttiker theory: When the photon energy exceeds the quantum dot resonance linewidth, degeneracy-dependent plateaus emerge. These are reproduced by sequential tunneling calculations. In the other case with large asymmetry in the tunnel couplings, the high-frequency response is two orders of magnitude larger than the low-frequency conductance G, favoring the high-frequency readout.

DOI: 10.1103/PhysRevB.108.205417

I. INTRODUCTION

The ability to detect single electrons in the solid state is useful for a variety of applications, including spin qubit readout [1–4], electrical current and capacitance standards [5,6], studying Cooper pair breaking [7–9], single-shot photodetection [10–13], and nanothermodynamics and fluctuations [14–19]. While many methods exist to detect charge, one of the main ways is to utilize quantum dots (QDs). These systems make excellent charge detectors due to their high sensitivity and well-established transport theory [20,21], allowing detectors to be made predictable with a well-understood operation principle. Originally, measurements were performed at DC, relying on a difference in current for the readout, resulting in a bandwidth up to some kilohertz [6,22]. In the last two decades, the readout methods have moved towards measuring the reflected power in a high-frequency tank circuit with resonant frequency in the 100 MHz to 1 GHz range. This results in bandwidths in the megahertz range, allowing for microsecond time resolution [23–25]. The response of the system in these studies is still governed by the low-frequency response of the system; that is, the admittance $Y(\omega)$ is equal to the DC conductance G of the system. In this paper, we increase the QD sensor frequency to the 4–8 GHz frequency range, where the cavity photon energy $\hbar\omega$ is greater than the thermal energy kT [26]. This opens up an avenue to increase the bandwidth correspondingly by an order of magnitude, possibly yielding a time resolution sufficient to probe the electron position in double-QD systems within the recently achieved coherence times [27,28]. Pioneering works at these frequencies have observed good agreement with the low-frequency result [29,30] or have considered primarily the dispersive effects motivated mostly by quantum capacitance effects [31]. In this paper, we focus on the dissipative part that yields a stronger response, making it useful for charge readout [26]. We present experimental results for two devices and show for both of them that at sufficiently high tunnel couplings such that the states are lifetime broadened, $\Gamma > kT$, the low-frequency result of $Y(\omega) = G$ still applies. However, when the device is tuned to the thermally broadened limit where the tunnel couplings $\Gamma < kT$, the measured admittance is qualitatively different from the DC conductance, displaying a linewidth of $2\hbar\omega$ in the QD level tuning and a factor of 2 difference in admittance depending on the direction of the level shift of the quantum dot relative to the leads ε, attributed to spin degeneracy. These results are well captured by sequential tunneling theory, directly evaluating the admittance for a QD subjected to a time-periodic drive [32], or using $P(E)$ theory, in which the admittance is inferred from the absorption in the cavity [33,34]. Last, we show, in line with Ref. [26], that in the other device with asymmetric tunnel couplings, the AC response

---

[*] harald.havir@ftf.lth.se

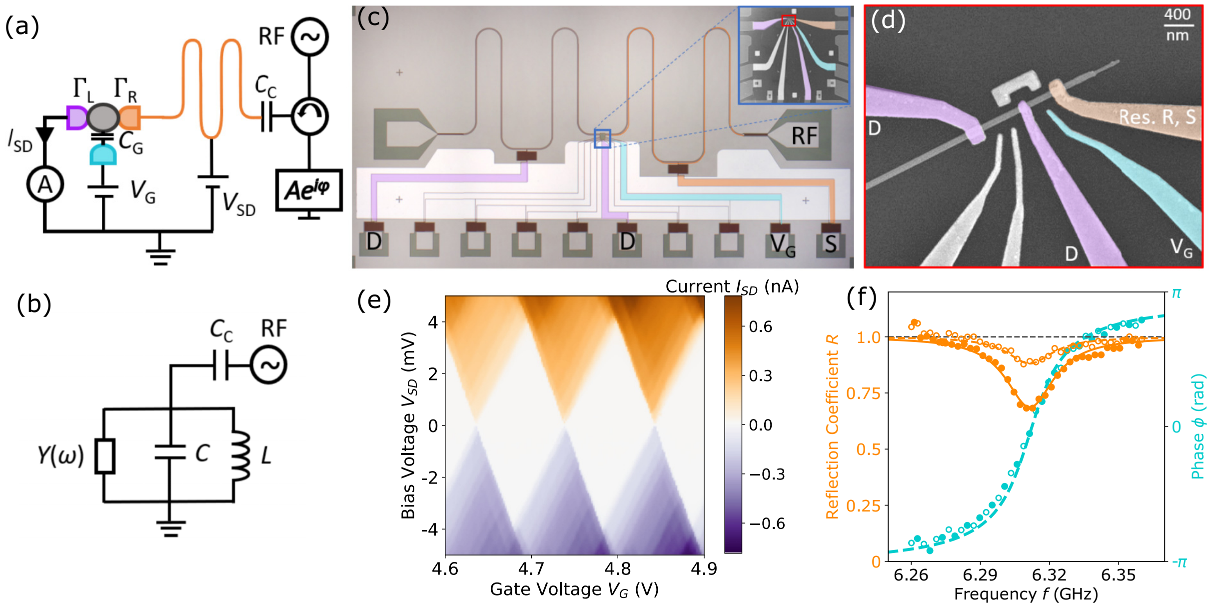

FIG. 1. (a) A schematic diagram of the studied device. A microwave resonator (orange) is driven with a high-frequency signal (RF) through the coupling capacitor C_C, and the reflected amplitude A and phase ϕ are measured. A QD with tunnel couplings Γ_R and Γ_L connects to the resonator via the source contact. The DC electrical current I_{SD} is measured from the drain contact, and DC voltage bias V_{SD} is applied via the resonator and a gate voltage V_G via a separate gate electrode. (b) The equivalent lumped-element LC circuit for the device with the complex admittance $Y(\omega)$ arising from the QD. (c) An optical micrograph of the device. The microwave resonator and DC lines are defined using a Nb etch-back method. The DC lines are capacitively shunted towards the resonator with a 30 nm aluminum oxide–50 nm aluminum stack (white area). The contacts near the QD, visible in the scanning electron micrograph in the inset, are defined using EBL and deposited using Ni/Au evaporation. (d) A close-up of (c) showing the InAs nanowire QD device. (e) The measured detector current I_{SD} as a function of bias and gate voltages V_{SD} and V_G. (f) Measured reflection coefficient R and phase ϕ as a function of frequency f with the QD in Coulomb blockade (open circles) and conducting at zero bias voltage (solid circles) at $V_G = 4.72$ V. Solid lines are fits to Eq. (1) with $f_r = 6.315$ GHz, $\kappa_C/2\pi = 22.3$ MHz, and $\kappa_{QD} = 0$ for Coulomb blockade and $\kappa_{QD}/2\pi = 2.1$ MHz for the QD in resonance.

remains large, while the DC transport is suppressed. Here the response of our device with lifetime broadening falls into a regime where neither noninteracting scattering theory nor sequential tunneling models are applicable.

II. DEVICE CONFIGURATION

The main device used to perform measurements is illustrated schematically in Fig. 1(a). The device builds on a transmission line resonator, shown in orange, which for the fundamental mode is equivalent to the LC circuit in Fig. 1(b). The right end of the resonator is connected to an input line via a coupling capacitor C_C, which allows the measurement of the amplitude and phase of a reflected signal. The left end of the resonator, on the other hand, couples to a QD via the right junction capacitance. This configuration makes the QD source-drain transport admittance $Y(\omega)$ appear directly on the LC resonator. At low drive frequency $\omega = 2\pi f$, this admittance is given by just the DC conductance G, i.e., $Y(\omega) = G$, and the QD gives rise to dissipation in the resonator.

The reflection coefficient of the input port is given by (see Appendix A)

$$R = 1 - \frac{(\kappa_{QD} + \kappa_i)\kappa_C}{(\kappa/2)^2 + (\omega - \omega_r - \delta\omega_{QD})^2}, \qquad (1)$$

where $\omega_r = 1/\sqrt{LC}$ is the resonance frequency, $\kappa = \kappa_{QD} + \kappa_i + \kappa_C$ the sum of all the couplings defining the linewidth of the resonance, κ_i is the internal losses, $\kappa_C = Z_0\omega^2 C_C^2/C$ is the input coupling [35], and $\kappa_{QD} = \mathrm{Re}[Y(\omega)]/C$ is the QD coupling strength. The term κ_{QD} is directly proportional to the admittance $\mathrm{Re}[Y(\omega)]$; determining κ_{QD} from a change in the measured reflection coefficient R thus allows us to determine the dissipative part of the QD response $\mathrm{Re}[Y(\omega)]$. On the other hand, $\mathrm{Im}[Y(\omega)]$ gives rise to a dispersive shift $\delta\omega_{QD} = \mathrm{Im}[Y(\omega)]/2C$ in Eq. (1), which results in a change in the resonance frequency. These dispersive shifts are typically small, of the order of $10^{-3}\omega_r$, which is also the case for our devices, and have been studied in detail for QDs coupled capacitively via a gate electrode [31].

To measure the DC conductance G of the QD at the same operation point as $Y(\omega)$, we apply a DC bias voltage V_{SD} to the voltage node point in the middle of the $\lambda/2$ resonator such that it does not disturb the resonance but instead appears at the source contact of the QD [12,31]. The current I_{SD}, measured from the drain contact, then yields the conductance $G = dI_{SD}/dV_{SD}$ and enables the comparison of this low-frequency transport result to the high-frequency admittance $Y(\omega)$. These DC lines, in addition to a gate line with applied gate voltage V_G to change the electron number in the QD, are shunted with a large capacitor to ground to prevent microwaves from leaking out from the lines.

The physical realization of the device is presented in Fig. 1(c). The coplanar waveguide, highlighted in orange, is a 9.86 mm long metallic strip with a width of 10 μm and a gap of 5 μm to the ground plane. Based on Ref. [35], we estimate the lumped-element capacitance $C = 765$ fF and inductance $L = 871$ pH, giving a characteristic impedance $Z_0 = \pi/2\sqrt{L/C} = 53\ \Omega$, where the factor of $\pi/2$ appears from the mapping from distributed to lumped elements [35]. An RF port is connected to the resonator with a 400 μm long two-finger geometry capacitor which defines the input coupling κ_C. The QD forms in an epitaxially grown InAs nanowire [see Fig 1(d)] by altering the growth between zinc blende (ZB) and wurtzite (WZ) crystal phases [36]. The WZ segments have a conduction band offset of 135 meV compared to the ZB segments [37], forming tunnel barriers, and a ZB segment between the barriers defines a QD with a length of 130 nm and a diameter of 80 nm [38]. The location of these barriers is discerned by selectively growing GaSb on the ZB segments, which highlights the features of the QD [39]. The offset between ZB and WZ allows the atomically sharp definition of barriers, leading to a well-defined QD. The DC lines are capacitively shunted by growing a 30 nm thick aluminum oxide layer with atomic layer deposition and evaporating a 50 nm thick aluminum film in the light-gray area in Fig 1(c). Additional inductive filtering is added to all the DC pads as well as the midpoint connections to reduce RF leakage [40]. The device is bonded to a printed circuit board and measured in a dilution refrigerator at an electronic temperature of $T = 50$ mK at base temperature. Figure 1(e) shows the measured Coulomb diamonds exhibiting a charging energy $E_C = 3.5$ meV and excited states with energies around 300 μeV. The lever arm to the gate, $\alpha = 0.03$ eV/V, is also determined.

Figure 1(f) presents the resonator response with the QD in Coulomb blockade (CB) and in the conduction resonance at $V_G = 5.9$ V, which is attained with an input power $P = -130$ dBm to the resonator. With the QD transport suppressed in CB (open circles), we determine the bare resonator properties by fitting these data to Eq. (1) with $\kappa_{QD} = 0$ and $\delta\omega_{QD} = 0$. We obtain the resonance frequency $f_r = 6.318$ GHz and determine the coupling strengths $\kappa_C/2\pi = 22.3$ MHz and $\kappa_i/2\pi = 0.7$ MHz. The phase response (cyan circles) shows a 2π winding, characteristic of an overcoupled resonator. Next, the QD is tuned to resonance, and the measurements are repeated. The corresponding data (solid circles) demonstrate that the linewidth of the resonance increases due to additional absorption in the QD. The reduction in amplitude also reflects the increase in total dissipation in the resonator by κ_{QD}. Keeping the resonator parameters acquired from the previous data set fixed, the fit to Eq. (1) is now repeated, providing $\kappa_{QD}/2\pi = 2.1$ MHz and vanishing $\delta\omega_{QD}$.

III. COMPARISON OF CONDUCTANCE AND HIGH-FREQUENCY ADMITTANCE

Now we turn to comparing the low-frequency conductance G and the high-frequency response $Y(\omega)$ presented in Figs. 2(a) and 2(b) for a lifetime-broadened resonance at $V_G = 6.7$ V. The QD conductance G has a peak width of 60 μeV $>$ 4 kT; hence, a fit (solid line) to Landauer-Büttiker theory [21] yields the tunnel couplings $\Gamma_L = 6$ μeV and $\Gamma_R = 55$ μeV. In Fig. 2(b) the measured admittance $\mathrm{Re}[Y(\omega)] = \kappa_{QD}C$ is shown for the same resonance with an input power $P = -120$ dBm. This admittance response is identical to the DC conductance G within 30%, as expected from the low-frequency prediction of $Y(\omega) \approx G$. A numerical calculation based on Landauer-Büttiker theory (orange line) for this system (see Appendix B and Ref. [41]) also predicts the equivalence $\mathrm{Re}[Y(\omega)] = G$ for this configuration. The deviation from the theoretical prediction could arise from spin degeneracy effects similar to those in Fig. 2(d) or could be due to a spurious coupling between the resonator and a nearby charge state [42].

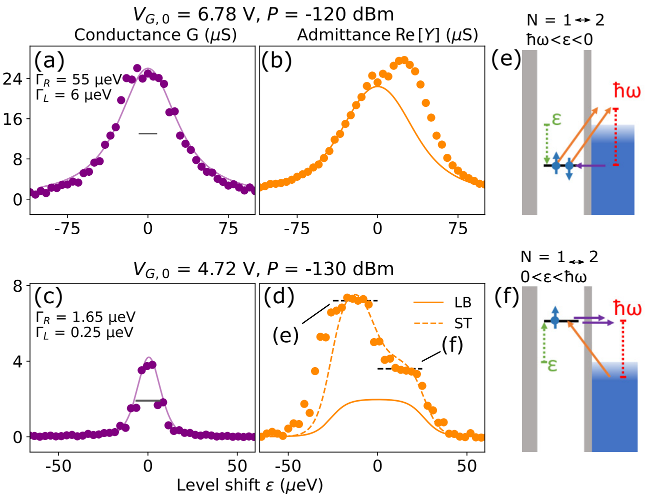

FIG. 2. (a) The DC conductance G measured at zero bias ($V_{\mathrm{SD}} = 0$) as a function of the level shift $\epsilon = -\alpha(V_{\mathrm{G}} - V_{\mathrm{G0}})$ for the QD resonance at $V_{\mathrm{G0}} = 6.78$ V without applying the RF drive. An additional gate voltage $V_{\mathrm{G},2} = 0.5$ V is applied to the two remaining gate contacts in order to tune the tunnel couplings of the single dot slightly (set to 0 V in subsequent measurements). The solid purple line shows a fit to Landauer-Büttiker (LB) theory, Eq. (B17), while the solid black line indicates the linewidth of a thermally broadened peak (4 kT). (b) The admittance data $\mathrm{Re}[Y(\omega)]$ around the same resonance as in (a). The solid orange line is the finite-frequency Landauer-Büttiker theory in Eq. (B15). (c) and (d) Data for another resonance at $V_{\mathrm{G0}} = 4.72$ V. The fit in (c) is done using Eq. (C12), and in (d) the dashed orange line is a sequential tunneling (ST) calculation of Eq. (C13) based on the formalism in Ref. [32], while the dashed black lines indicate the photon energy. (e) and (f) Band diagrams with the two energy level shift ε directions indicated in (d). The lines indicate the photon energy (dotted red), the level shift ε due to the applied gate voltage (dashed green), and the transport processes due to photon-assisted tunneling (solid orange upwards arrows) and regular tunneling (solid purple horizontal arrows). The number of orange arrows specifies the number of electrons which can participate in the corresponding tunneling process between the $N = 1$ and $N = 2$ electrons on the dot.

The energy of a single microwave photon is $\hbar\omega_{\mathrm{r}} = 26$ μeV; hence, in the configuration in Figs. 2(a) and 2(b) the lifetime broadening exceeds the photon energy. With a reduction in the gate voltage, the tunnel coupling decreases, reducing the lifetime broadening. This allows us to make the linewidth of the DC conductance peak smaller than the photon energy. Tuning from $V_G = 6.78$ V to $V_G = 4.72$ V results in a thermally broadened peak, as shown in Fig. 2(c). Note that here the clustering of data points is likely a consequence of a noisy voltage source because it is operated at its resolution limit. The Landauer-Büttiker theory fit again reproduces the results with $\Gamma_L = 0.25\,\mu\text{eV}$. As the linewidth is now set by temperature and not the tunnel couplings, the larger coupling may vary from $\Gamma_R = 0.5$ to $6\,\mu\text{eV}$ without disrupting the fit to the data. Now the measured $Y(\omega)$, presented in Fig. 2(d), shows a broader peak with a qualitatively different peak shape than the conductance has; hence, the equivalence $Y(\omega) = G$ is broken. The response has two plateaus at 3.6 and 7.2 µS, extending out by ~30 µeV in either direction from the midpoint and matching the photon energy in line with the DC response studied in Ref. [43]. The broadening of $Y(\omega)$ arises since with the energy of the photon, the system overcomes an additional charging energy cost up to $\hbar\omega_r$, as depicted in Figs. 2(e) and 2(f).

The admittance for each level shift polarity within the energy window is constant. This admittance is directly proportional to the tunneling rate due to photon absorption, which is proportional to the number of available states in the metallic leads. Thus, tuning the level shift within the energy window probes changes in the density of states in the leads. The flat plateaus observed in Fig. 2(d) therefore indicate a constant density of states in the leads, as expected for a metal within a narrow energy range [44]. The factor of 2 difference between level shift directions arises from the spin degeneracy in the QD. The photon absorption rate is two times higher for tunneling out of the QD (which applies for $\epsilon > 0$) compared to tunneling into the QD (which applies for $\epsilon < 0$). As the Landauer-Büttiker model [solid line in Fig. 2(d)] does not account for spin effects in the quantum dot system the predicted response is inaccurate, capturing only the broadening of the line due to the photon energy and failing to capture the two plateaus that appear in the data. Instead, a sequential tunneling (ST) model with either time-dependent voltage drive [32] or $P(E)$ theory [33,34] describes the full response more accurately in this regime. The two ST models agree at weak resonator-QD couplings, but as the coupling increases (e.g., with increasing cavity impedance), the $P(E)$ theory predicts spontaneous emission events which further change the transport. See Appendixes C and D for details. Here we have fitted the value of the larger tunneling rate to $\Gamma_R = 1.65$ µeV, which sets the overall height of the response. The spin degeneracy shifts the resonance point and the total height of the resonance peak by a small amount [see Eq. (E6)]; thus, the DC fitting parameter values were adjusted to $\Gamma_L = 0.25$ µeV and $\alpha\Delta V_{G0} = -1.5$ µeV.

Figure 3 extends the measurements of Figs. 2(c) and 2(d) as a function of drive power P. At low drives $P < -100$ dBm, the linewidth of $Y(\omega)$ is essentially set by $2\hbar\omega_r$, while the linewidth of G remains thermally broadened for $P < -120$ dBm. At high power additional broadening is observed in both the DC and RF results, in line with the previous work in Refs. [45,46]. The amplitude of the microwave oscillations inside the resonator is estimated by following the steps in Refs. [47,48], yielding the microwave amplitude

$$V_{\text{MW}} = \left(\frac{4Q^2 Z_0}{Q_{\text{ext}}}P\right)^{-1/2}. \qquad (2)$$

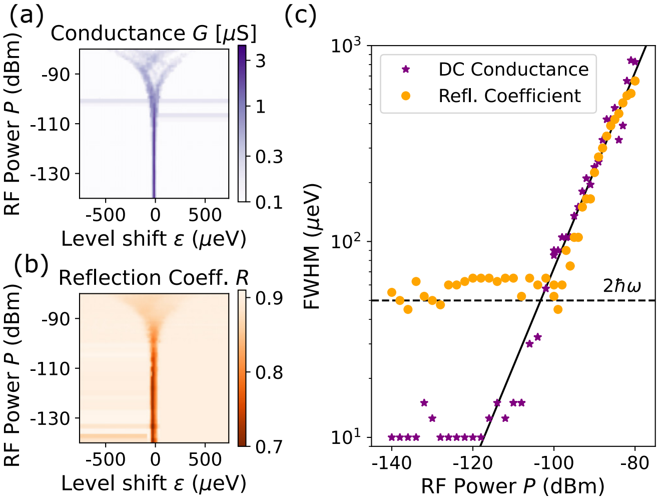

FIG. 3. (a) The DC conductance and (b) reflection coefficient of the microwave cavity are measured simultaneously as the microwave power to the resonator input is changed. (c) The measured linewidths, along with a dashed black line indicating $2\hbar\omega_r$ and a solid black line corresponding to the calculated microwave amplitude in Eq. (2).

With characteristic impedance $Z_0 = \pi/2\sqrt{L/C} = 53\ \Omega$, quality factor $Q = \omega_r/\kappa = 262$, and external quality factor $Q_{\text{ext}} = 270$, we obtain the solid line in Fig. 3(c). As the voltage amplitude V_{MW} enters the high-power regime, the broadening of the RF and DC responses both arise from the amplitude of the microwave signal. For the microwave response, the boundary point $P \approx -100$ dBm between the high- and low-power regimes is set by the condition $eV_{\text{MW}} = \hbar\omega_r$, i.e., whether the energy related to the amplitude or single photon is dominant. However, the width of the DC feature continues to be defined by the drive amplitude until the power $P = -120$ dBm, at which point the energy corresponding to the drive amplitude becomes smaller than the thermal energy, i.e., $eV_{\text{MW}} < kT$. The measurements of $Y(\omega)$ performed in the measurements in Fig. 2 were performed at $P \leqslant -120$ dBm, allowing high-power effects to be ignored in the analysis. Note also that the DC measurements in Fig. 2 were performed without applied microwave drive, although applying the drive does not change the DC response at this power level.

Figures 4(a) and 4(b) repeat the study in the lifetime-broadened case for a second device. Now we have a much more asymmetric device with fitted values of $\Gamma_L = 1.4$ µeV and $\Gamma_R = 357.5$ µeV, reaching again the equivalence $Y(\omega) = G$, valid in both experiment and theory. Tuning the QD to a lower gate voltage $V_{G_0} = 6.73$ V [Figs. 4(c) and 4(d)] again has the effect of reducing the tunnel barriers such that the conductance G is suppressed by two orders of magnitude. This results in a correspondingly smaller $\Gamma_L = 6.7$ neV, while the right barrier $\Gamma_R = 80$ µeV still provides a lifetime broadening to the system. In the measured high-frequency response, we observe a peak with the same linewidth as the DC feature but with an amplitude value of $Y(\omega)|_{\epsilon=0} = 3.6$ µS, which is two orders of magnitude greater than the peak value of the DC conductance of 30 nS. In this case, Landauer-Büttiker theory still predicts $Y(\omega) = G$. Therefore, the linewidth of $Y(\omega)$ in Fig. 4(d) is reproduced correctly, but the predicted overall

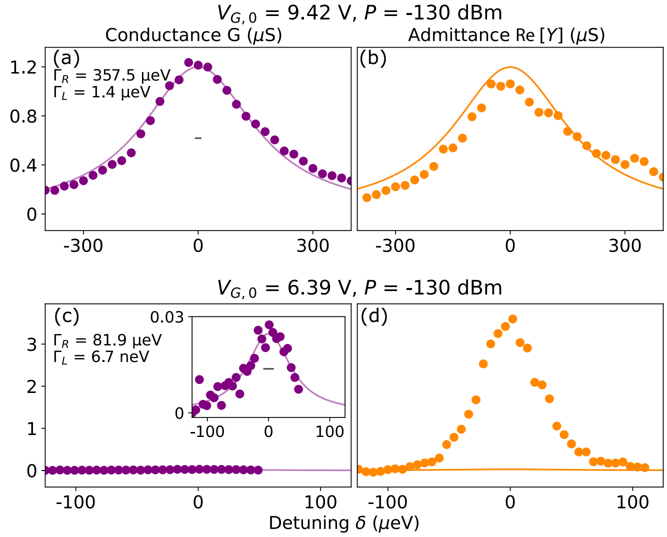

FIG. 4. The same measurements as in Fig. 2 for a second device at (a) and (b) $V_{\mathrm{G0}} = 9.4$ V and (c) and (d) $V_{\mathrm{G0}} = 6.4$ V. For the second QD, the charging energy and lever arm are $E_C = 2$ meV and $\alpha = 0.04$ eV/V.

magnitude is two orders of magnitude lower than the measured response. The sequential tunneling calculations miss lifetime-broadening effects and thus does not replicate the linewidth. The predicted peak admittance of $Y(\omega) = 30$ μ S, on the other hand, predicts qualitatively correctly that the RF response is stronger, although the predicted value is an order of magnitude larger than the measured one. With these arguments and findings, we interpret that the correct picture to describe is closer to the sequential tunneling case in Ref. [49]: Here the junction capacitances determine how the microwave drive is divided between the junctions, independent of the junction transparency. We take the two junction capacitances to be comparable as they depend inversely on the barrier thickness compared to the much stronger exponential dependence of the tunnel couplings. Also, based on the Coulomb oscillation period, the gate capacitance is much smaller than the junction capacitances. Therefore, the AC drive is evenly divided across the two junctions and gives rise to considerable drive and dissipation at the transparent junction. This is in stark contrast to DC transport, in which most of the voltage signal is across the opaque barrier. Such an enhanced RF response was observed before both in single-dot devices [26] and for double quantum dots [31,50] in which one dot in CB blocks transport from one side. However, because our device operates in the lifetime-broadened regime, a more advanced theory combining the strong tunnel coupling with spin and charging effects [49] that is beyond the scope of this work would be needed to fully explain the response.

IV. CONCLUSIONS

In summary, we studied the high-frequency source-drain response of a quantum dot. We showed experimentally that the low-frequency result of $Y(\omega) = G$ holds for quantum dots tuned to sufficiently large tunnel couplings in line with the slow-drive limit. However, when the tunnel couplings are tuned to be smaller than the photon energy, the measured linewidth of the admittance $Y(\omega)$ is set by the photon energy. This response is well described by sequential tunneling theory, taking into account spin effects of the quantum dot, which are not properly accounted for in Landauer-Büttiker formalism. Additionally, the low-frequency limit does not hold when the drive amplitude is made sufficiently large or there is large asymmetry in tunnel couplings of the junctions. For the highly asymmetric case, it was also shown that the admittance $Y(\omega)$ can be orders of magnitude larger than the conductance G, indicating a potential benefit of measuring at high frequencies, as the readout strength remains large even for weakly coupled quantum dots.

ACKNOWLEDGMENTS

We are thankful for financial support from the Foundational Questions Institute, a donor-advised fund of the Silicon Valley Community Foundation (Grant No. FQXi-IAF19-07), the Knut and Alice Wallenberg Foundation through the Wallenberg Center for Quantum Technology (WACQT), the Swedish Research Council (Dnr 2019-04111), and NanoLund.

APPENDIX A: LUMPED-ELEMENT CIRCUIT AND MICROWAVE REFLECTION PROBABILITY

The QD-resonator system, linearly driven at a frequency ω close to resonance, is modeled as a lumped-element circuit, as shown in Fig. 1(b). The resonator is described by an inductance L and capacitance C, and internal losses are accounted for by a resistance R_i. The QD has a frequency-dependent complex admittance $Y(\omega)$. The resonator is coupled to an input transmission line, with impedance Z_0, via a coupling capacitance C_{C}. The total impedance $Z(\omega)$ of the circuit is then given by

$$Z = \frac{1}{i\omega C_{\mathrm{C}}} + \left(Y(\omega) + 1/R_i + i\omega C + \frac{1}{i\omega L}\right)^{-1} \equiv Z_{\mathrm{R}} + iZ_{\mathrm{I}}. \tag{A1}$$

Writing $\omega_r = 1/\sqrt{LC}$, $\kappa_{\mathrm{i}} = R_i/C$, $\kappa_{\mathrm{QD}} = \mathrm{Re}[Y(\omega)]/C$, and $\delta\omega_{\mathrm{QD}} = \mathrm{Im}[Y(\omega)]/(2C)$ and using the fact that $\omega \approx \omega_r$, we can write the real and imaginary parts of the impedance as

$$\begin{aligned} Z_{\mathrm{R}} &= \frac{(\kappa_{\mathrm{QD}} + \kappa_i)/(4C)}{(\kappa_{\mathrm{QD}} + \kappa_i)^2/4 + (\omega - \omega_{\mathrm{r}} + \delta\omega_{\mathrm{QD}})^2} \\ Z_{\mathrm{I}} &= -\left(\frac{1}{\omega_{\mathrm{r}} C_{\mathrm{C}}} + \frac{(\omega - \omega_{\mathrm{r}} + \delta\omega_{\mathrm{QD}})/C}{(\kappa_{\mathrm{QD}} + \kappa_i)^2/4 + (\omega - \omega_{\mathrm{r}} + \delta\omega_{\mathrm{QD}})^2}\right). \end{aligned} \tag{A2}$$

The reflection probability R for a coherent microwave drive tone at ω is given by

$$R = \left|\frac{Z(\omega) - Z_0}{Z(\omega) - Z_0}\right|^2 = 1 - \frac{4Z_{\mathrm{R}}Z_0}{(Z_{\mathrm{R}} + Z_0)^2 + Z_{\mathrm{I}}^2}, \tag{A3}$$

and the corresponding reflection phase is

$$\phi = \mathrm{atan}\left(\frac{2Z_{\mathrm{I}}Z_0}{Z_{\mathrm{R}}^2 + Z_{\mathrm{I}}^2 - Z_0^2}\right). \tag{A4}$$

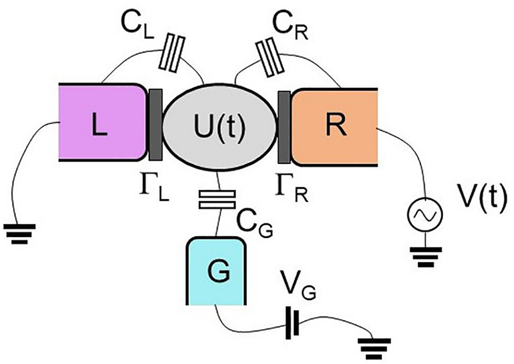

FIG. 5. Sketch of the quantum dot showing, in addition to Fig. 1 in the main text, the tunnel junction capacitances C_L and C_R and the applied potential $V(t)$ on the right contact and induced potential $U(t)$ in the QD.

For the reflection probability, inserting Z_R and Z_I into Eq. (A3), writing the capacitive coupling rate $\kappa_\mathrm{C} = Z_0\omega_r^2 C_\mathrm{C}^2/C$, and neglecting terms proportional to the small parameter $C_\mathrm{C}\omega_r Z_0 \ll 1$, we arrive at

$$R = 1 - \frac{(\kappa_\mathrm{QD} + \kappa_\mathrm{i})\kappa_\mathrm{C}}{(\kappa/2)^2 + (\omega - \omega_\mathrm{r}^* + \delta\omega_\mathrm{QD})^2}, \tag{A5}$$

where we introduced the total $\kappa = \kappa_\mathrm{QD} + \kappa_\mathrm{i} + \kappa_\mathrm{C}$ and $\omega_\mathrm{r}^* = \omega_r(1 + C_\mathrm{C}/C)$, the capacitive coupling renormalized resonance frequency. By noticing that $C_\mathrm{C}/C \ll 1$ we can put $\omega_\mathrm{r}^* \approx \omega_\mathrm{r}$, and we then arrive at Eq. (1) in the main text.

APPENDIX B: LANDAUER-BÜTTIKER FORMALISM

An extended sketch of Fig. 1(a) is presented in Fig. 5. It includes junction capacitances and potentials. In this Appendix, we calculate the QD admittance within the Landauer-Büttiker formalism. With this approach, the QD admittance $Y(\omega)$ is evaluated within a time-dependent scattering approach, neglecting Coulomb blockade effects but fully accounting for the current conservation at the QD via the flow of dynamic screening currents. Our result is an extension of the discussion presented by Prêtre, Thomas, and Büttiker [41], here including QD-lead capacitive couplings. We therefore present only the main steps in the derivation.

The starting point for the calculation is the energy-dependent, symmetric scattering matrix $S(E)$ of the QD, effectively assuming a single transport channel, given by

$$S(E) = \begin{pmatrix} r(E) & t'(E) \\ t(E) & r'(E) \end{pmatrix}, \tag{B1}$$

where the reflection and transmission amplitudes are given by the Breit-Wigner expressions

$$\begin{aligned} r(E) &= 1 - \frac{i\Gamma_\mathrm{L}}{E - \epsilon + i(\Gamma_\mathrm{L} + \Gamma_\mathrm{R})/2}, \\ r'(E) &= 1 - \frac{i\Gamma_\mathrm{R}}{E - \epsilon + i(\Gamma_\mathrm{L} + \Gamma_\mathrm{R})/2}, \\ t(E) = t'(E) &= \frac{i\sqrt{\Gamma_\mathrm{L}\Gamma_\mathrm{R}}}{E - \epsilon + i(\Gamma_\mathrm{L} + \Gamma_\mathrm{R})/2}. \end{aligned} \tag{B2}$$

Here $\epsilon = \epsilon_\mathrm{d} - \alpha V_\mathrm{G}$ is the energy of the discrete QD level, where ϵ_d is the bare dot energy and $\alpha = eC_\mathrm{G}/(C_\mathrm{L} + C_\mathrm{R} + C_\mathrm{G})$ is the lever arm for the gate potential V_G. Unprimed (primed) amplitudes correspond to particles incident from the left (right) lead.

We consider the case with a pure AC voltage $V(t) = V\cos(\omega t)$ at contact R, while contact L is grounded and the gate contact is kept at the constant potential V_G corresponding to the experimental settings. The case with a pure DC voltage bias is discussed below. As a result of the oscillating potential $V(t)$, a potential $U(t)$ is induced on the QD. The effect of the oscillating potentials is that electrons can pick up or loose quanta of energy $\hbar\omega$ when scattering at the QD.

Our focus is on the regime of weak microwave drive, where the response is linear in the potentials. In this regime $V \ll \hbar\omega$, and only a single quantum can be picked up or lost. As a consequence, the time-dependent particle current at lead L/R has only a single Fourier component,

$$I_\mathrm{L/R}(t) = I_\mathrm{L/R}(\omega)e^{i\omega t} + I_\mathrm{L/R}^*(\omega)e^{-i\omega t}. \tag{B3}$$

The current component $I_\mathrm{L/R}(\omega)$ can be expressed in terms of the scattering amplitudes in Eq. (B2) and the lead Fermi distribution $f(E)$ as

$$\begin{aligned} I_\mathrm{L}(\omega) = \frac{e^2}{h}\int dE\{&-[1 - r^*(E)r(E+\hbar\omega)]U(\omega) - t'^*(E)t' \\ &\times (E+\hbar\omega)[V(\omega) - U(\omega)]\}F(E,\omega) \end{aligned} \tag{B4}$$

and

$$\begin{aligned} I_\mathrm{R}(\omega) = \frac{e^2}{h}\int dE\{&[1 - r'^*(E)r'(E+\hbar\omega)][V(\omega) - U(\omega)] \\ &+ t^*(E)t(E+\hbar\omega)U(\omega)\}F(E,\omega), \end{aligned} \tag{B5}$$

where

$$F(E,\omega) = \frac{f(E) - f(E+\hbar\omega)}{\hbar\omega}, \quad f(E) = \frac{1}{1 + e^{E/k_\mathrm{B}T}}, \tag{B6}$$

and we have introduced the Fourier components $V(\omega)$ and $U(\omega)$ of the potentials $V(t)$ and $U(t)$. We note that $V(\omega) = V/2$, independent of ω, but the frequency-dependent notation is kept for convenience.

Inserting the scattering amplitude expressions in Eq. (B2) into the current components in Eqs. (B4) and (B5), we can write

$$I_\mathrm{L}(\omega) = G(\omega)\left[\frac{i\hbar\omega}{\Gamma_\mathrm{R}}U(\omega) - V(\omega)\right] \tag{B7}$$

and

$$I_\mathrm{R}(\omega) = G(\omega)\left[\frac{i\hbar\omega}{\Gamma_\mathrm{L}}U(\omega) + \left(1 - \frac{i\hbar\omega}{\Gamma_\mathrm{L}}\right)V(\omega)\right], \tag{B8}$$

where

$$G(\omega) = \frac{e^2}{h}\int dE\,\mathcal{T}(E,\omega)F(E,\omega) \tag{B9}$$

and

$$\begin{aligned} &\mathcal{T}(E,\omega) \\ &= \frac{\Gamma_\mathrm{L}\Gamma_\mathrm{R}}{E - \epsilon + i(\Gamma_\mathrm{L} + \Gamma_\mathrm{R})/2}\frac{1}{E + \hbar\omega - \epsilon - i(\Gamma_\mathrm{L} + \Gamma_\mathrm{R})/2}. \end{aligned} \tag{B10}$$

For nonzero frequencies, the particle currents flowing into the QD typically do not add up to zero, i.e., $I_{\rm L}(\omega) + I_{\rm R}(\omega) \neq 0$. As a consequence, there is nonzero charge $Q(t)$ on the QD dot, which induces AC screening, or displacement, currents flowing between the QD and the leads L and R as well as the gate G. The total screening current into the QD is given by $I_{\rm sc}(t) = dQ(t)/dt$, with the charge determined from classical electrostatic considerations, via the potentials $V(t)$ and $U(t)$ and the capacitances $C_{\rm L}$, $C_{\rm R}$, and $C_{\rm G}$. This gives the screening current Fourier component $I_{\rm sc}(\omega)$ as

$$I_{\rm sc}(\omega) = -i\omega[-U(\omega)(C_{\rm L} + C_{\rm R} + C_{\rm G}) + V(\omega)C_{\rm R}]. \tag{B11}$$

The induced QD potential $U(\omega)$ can then be determined using the condition that the total current flowing into the dot is conserved,

$$I_{\rm L}(\omega) + I_{\rm R}(\omega) + I_{\rm sc}(\omega) = 0, \tag{B12}$$

giving

$$U(\omega) = \frac{\Gamma_{\rm R}(\hbar G(\omega) + C_{\rm R}\Gamma_{\rm L})}{\hbar G(\omega)(\Gamma_{\rm L} + \Gamma_{\rm R}) + (C_{\rm L} + C_{\rm R} + C_{\rm G})\Gamma_{\rm R}\Gamma_{\rm L}} V(\omega). \tag{B13}$$

We note that in the limit $\omega \to \infty$, we have $G(\omega) \to 0$ and $U(\omega) = C_{\rm R}/(C_{\rm L} + C_{\rm R} + C_{\rm G})V(\omega)$, which is the purely capacitive voltage division. The sought admittance is given by

$$Y(\omega) = \frac{I_{\rm R}(\omega) - i\omega C_{\rm R}[V(\omega) - U(\omega)]}{V(\omega)}, \tag{B14}$$

the ratio of the total current, i.e., the sum of the particle and screening currents, flowing into the QD from contact R and the potential at R. Inserting the expression for $I_{\rm R}(\omega)$ in Eq. (B8) and $U(\omega)$ in (B13), we arrive at

$$Y(\omega) = G(\omega) - \frac{i\omega[\hbar G(\omega) + \Gamma_{\rm L}C_{\rm R}][\hbar G(\omega) + \Gamma_{\rm R}(C_{\rm L} + C_{\rm G})]}{\Gamma_{\rm L}\Gamma_{\rm R}(C_{\rm L} + C_{\rm R} + C_{\rm G}) + \hbar G(\omega)(\Gamma_{\rm L} + \Gamma_{\rm R})}. \tag{B15}$$

This is the expression used for the numerical evaluations in the main text.

For the lifetime-broadening cases $\Gamma_{\rm L} + \Gamma_{\rm R} \gg k_{\rm B}T$, effectively taking $T = 0$, we can evaluate the integral in Eq. (B9), giving

$$G(\omega) = \frac{e^2}{h} \frac{i\Gamma_{\rm L}\Gamma_{\rm R}}{\hbar\omega(\Gamma_{\rm L} + \Gamma_{\rm R} - i\hbar\omega)} \ln \left[\frac{\epsilon^2 + ([\Gamma_{\rm L} + \Gamma_{\rm R}]/2 - i\hbar\omega)^2}{\epsilon^2 + (\Gamma_{\rm L} + \Gamma_{\rm R})^2/4}\right]. \tag{B16}$$

We note that at $\omega \to 0$ we have $I_{\rm R}(0) = -I_{\rm L}(0) = G(0)V(0)$, where

$$G(0) = \frac{e^2}{h} \frac{\Gamma_{\rm L}\Gamma_{\rm R}}{\epsilon^2 + (\Gamma_{\rm L} + \Gamma_{\rm R})^2/4} \tag{B17}$$

is the known DC bias conductance, as expected.

APPENDIX C: SEQUENTIAL TUNNELING MODEL WITH PERIODIC VOLTAGE DRIVE IN THE CLASSICAL LIMIT

Another extensively used model to describe QD transport builds on sequential tunneling of the electrons. Within this model, charging effects are intrinsically accounted for, while the lifetime-broadening effects are neglected. This Appendix calculates the QD admittance $Y(\omega)$ within the sequential tunneling approach for an applied, time-periodic voltage $V(t) = V_{\rm DC} + V_{\rm AC}\sin(\omega t)$. We closely follow the work of Bruder and Schoeller [32], fully accounting for Coulomb blockade effects, and present only the main steps in the derivation. The starting point is a rate equation for the Fourier components of the probabilities $P_0(t)$ and $P_1(t)$ to have zero extra electrons or one extra electron on the dot. Writing the Fourier series

$$P_j(t) = \sum_{m=-\infty}^{\infty} \tilde{P}_j(m)e^{-im\omega t}, \quad j = 0, 1, \tag{C1}$$

and noting that $\tilde{P}_j^*(m) = \tilde{P}_j(-m)$, the rate equation can be written as

$$\begin{aligned} -im\hbar\omega\tilde{P}_0(m) =& N(\Gamma_{\rm L} + \Gamma_{\rm R})\tilde{P}_1(m) \\ &- \sum_{\alpha=L,R}\sum_{n=-\infty}^{\infty} A^\alpha_{nm}[\tilde{P}_0(n) + N\tilde{P}_1(n)], \end{aligned} \tag{C2}$$

where

$$\begin{aligned} A^\alpha_{nm} &= F^\alpha_{n,m} + \left(F^\alpha_{-n,-m}\right)^*, \; F^\alpha_{nm} \\ &= \frac{i^{m-n}}{2}\sum_{k=-\infty}^{\infty} J_{k+n}\left(\frac{eV_\alpha}{\hbar\omega}\right) J_{k+m}\left(\frac{eV_\alpha}{\hbar\omega}\right) f_\alpha(\epsilon_k), \end{aligned} \tag{C3}$$

$J_n(x)$ is the Bessel function, $f_\alpha(\epsilon_k)$ is the Fermi function of lead $\alpha = L, R$ (incorporating the DC bias $V_{\rm DC}$ at contact R), and $\epsilon_k = \epsilon + k\hbar\omega$, with ϵ being the dot energy. The AC potential drops $V_{\rm L/R}$ across the L and R barriers are $V_{\rm L} = -U$ and $V_{\rm R} = V_{\rm AC} - U$, where $U = V_{\rm AC}C_{\rm R}/(C_{\rm R} + C_{\rm L})$ is the amplitude of the induced dot potential. Here we have assumed $C_G \ll C_{\rm R}, C_{\rm L}$, which is the case for the studied devices. The integer N arises from the degeneracy of the QD energy level [16,51]; that is, it sets the number of possible charge states in the dot, effectively multiplying the out tunneling rates. For our spin-degenerate QD we have $N = 2$. The probability conservation condition, from $P_0(t) + P_1(t) = 1$ for any t, further gives

$$\tilde{P}_0(m) + \tilde{P}_1(m) = \delta_{m0}. \tag{C4}$$

The Fourier component of the particle current $I_\alpha(t)$ in lead α is given by

$$\tilde{I}_\alpha(m) = \frac{e\Gamma_\alpha}{\hbar}\left(N\tilde{P}_1(m) - \sum_{n=-\infty}^{\infty} A^\alpha_{nm}[\tilde{P}_0(n) + N\tilde{P}_1(n)]\right). \tag{C5}$$

As in the lifetime-broadened limit, the total current is obtained by the sum of the particle currents and the displacement, or screening, currents. However, as pointed out in Ref. [32], the screening currents are typically very small in Coulomb blockaded systems, and we neglect them here. This gives the expression for the Fourier components of the total current,

$$\tilde{I}(m) = \frac{C_{\rm R}}{C_{\rm L} + C_{\rm R}}\tilde{I}_{\rm L}(m) - \frac{C_{\rm L}}{C_{\rm L} + C_{\rm R}}\tilde{I}_{\rm R}(m), \tag{C6}$$

which is valid for arbitrary drive amplitude and frequency.

Like for the Landauer-Büttiker theory in Appendix B, we focus on the regime of small AC driving amplitude, $eV_{\mathrm{AC}} \ll \hbar\omega$. Expanding the Bessel functions J_n in the argument $eV_{\mathrm{AC}}/(\hbar\omega)$, and writing the probabilities $\tilde{P}_j(m) = \tilde{P}_j^{(0)}(m) + (eV_{\mathrm{AC}}/[\hbar\omega])\tilde{P}_j^{(1)}(m) + \cdots$, we can solve Eq. (C2) order by order in $eV_{\mathrm{AC}}/(\hbar\omega)$. To evaluate the DC $\tilde{I}(0)$ (in the absence of AC drive) as well as the first AC component $\tilde{I}(1)$, we need only the nonzero probability components $\tilde{P}_j^{(0)}(0) = 1 - \tilde{P}_1^{(0)}(0)$ (at $V_{\mathrm{AC}} = 0$) and $\tilde{P}_j^{(1)}(1) = -\tilde{P}_1^{(1)}(1)$ (at $V_{\mathrm{DC}} = 0$), given by

$$\tilde{P}_0^{(0)}(0) = \frac{N[\Gamma_{\mathrm{L}}(1-f_{\mathrm{L}}) + \Gamma_{\mathrm{R}}(1-f_{\mathrm{R}})]}{\Gamma_{\mathrm{L}} f_{\mathrm{L}} + \Gamma_{\mathrm{R}} f_{\mathrm{R}} + N[\Gamma_{\mathrm{L}}(1-f_{\mathrm{L}}) + \Gamma_{\mathrm{R}}(1-f_{\mathrm{R}})]}, \tag{C7}$$

where, for brevity, we write $f_{\mathrm{L}} = f_{\mathrm{L}}(\epsilon)$, $f_{\mathrm{R}} = f_{\mathrm{R}}(\epsilon)$, and

$$\tilde{P}_0^{(1)}(1) = \frac{-ie}{2\hbar\omega}\frac{[\Gamma_{\mathrm{L}} V_{\mathrm{L}} + \Gamma_{\mathrm{R}} V_{\mathrm{R}}]}{(\Gamma_{\mathrm{L}} + \Gamma_{\mathrm{R}})[N + (1-N)f(\epsilon)] - i\hbar\omega} \times \left[N + (1-N)\tilde{P}_0^{(0)}(0)\right][f(\epsilon_1) - f(\epsilon_{-1})]. \tag{C8}$$

Within the same small-amplitude approximation we have the current components

$$\tilde{I}_\alpha(0) = \frac{e\Gamma_\alpha}{\hbar}\left\{N\tilde{P}_1^{(0)}(0) - f_\alpha\left[N + (1-N)\tilde{P}_0^{(0)}(0)\right]\right\} \tag{C9}$$

and

$$\tilde{I}_\alpha(1) = \frac{e\Gamma_\alpha}{\hbar}\left\{-[N + (1-N)f(\epsilon)]\tilde{P}_0^{(1)}(1) - \frac{ieV_\alpha}{2\hbar\omega}[N + (1-N)\tilde{P}_0^{(0)}(0)][f(\epsilon_1) - f(\epsilon_{-1})]\right\}. \tag{C10}$$

Inserting the expressions for the probabilities and noting that $\tilde{I}_{\mathrm{L}}(0) = -\tilde{I}_{\mathrm{R}}(0)$, the DC becomes

$$\tilde{I}(0) = e\frac{N\Gamma_{\mathrm{L}}\Gamma_{\mathrm{R}}}{\Gamma_{\mathrm{L}} + \Gamma_{\mathrm{R}}}\frac{f_{\mathrm{R}} - f_{\mathrm{L}}}{(1-N)(f_{\mathrm{L}}\Gamma_{\mathrm{L}} + f_{\mathrm{R}}\Gamma_{\mathrm{R}}) + N(\Gamma_{\mathrm{R}} + \Gamma_{\mathrm{R}})}. \tag{C11}$$

Expanding the Fermi distributions to first (linear) order in the DC bias voltage, we arrive at the linear conductance

$$G = \tilde{I}(0)/V_{\mathrm{DC}} = -\frac{e^2}{2\pi}\frac{N\Gamma_{\mathrm{L}}\Gamma_{\mathrm{R}}}{\Gamma_{\mathrm{L}} + \Gamma_{\mathrm{R}}}\frac{df(\epsilon)}{d\epsilon}\frac{1}{N + (1-N)f(\epsilon)}, \tag{C12}$$

which is the expression used in the plot in Fig. 2(c) in the main text. With $N = 1$, this expression matches the standard nondegenerate result, found, e.g., in Ref. [52], and the Landauer-Büttiker result in the limit of $\Gamma_{\mathrm{L}} + \Gamma_{\mathrm{R}} \ll k_{\mathrm{B}}T$ and $\omega \to 0$.

For the AC, we can write $\tilde{I}(1) = iY(\omega)V_{\mathrm{AC}}/2$, with the admittance ($C_\Sigma = C_{\mathrm{L}} + C_{\mathrm{R}}$)

$$Y(\omega) = \frac{e^2}{2\pi}\frac{N[f(\epsilon_1) - f(\epsilon_{-1})]}{\hbar\omega[N + f(\epsilon)(1-N)]} \times \frac{\Gamma_{\mathrm{L}}\Gamma_{\mathrm{R}}[N + f(\epsilon)(1-N)] - i\hbar\omega\left[\Gamma_{\mathrm{L}}\frac{C_{\mathrm{R}}^2}{C_\Sigma^2} + \Gamma_{\mathrm{R}}\frac{C_{\mathrm{L}}^2}{C_\Sigma^2}\right]}{\{(\Gamma_{\mathrm{L}} + \Gamma_{\mathrm{R}})[N + (1-N)f(\epsilon)] - i\hbar\omega\}}, \tag{C13}$$

which is the expression used for the fit of Fig. 2(d) in the main text. We note that for $\omega \to 0$ we have $Y(0) = G$, as expected.

APPENDIX D: SEQUENTIAL TUNNELING MODEL WITH $P(E)$ THEORY

The sequential tunneling model in Appendix C treats the voltage drive $V(t)$ as a purely classical signal. Here we briefly consider another sequential tunneling model approach, the $P(E)$ theory, which treats the voltage in the resonator quantum mechanically. To calculate the electron and photon transport properties of the studied system within the $P(E)$ theory, we follow the formalism of Refs. [33,34,53]. In the presence of a photon environment, the tunneling rate Γ_+ into the quantum dot (QD) from an electronic reservoir and the opposite rate Γ_- out from it [16,51] are convoluted with the probability $P(E)$ to absorb energy E from the environment. The resulting tunneling rates for left, $i = L$, and right, $i = R$, tunnel junctions are

$$\Gamma_{i+}(\varepsilon_i) = \frac{\Gamma_i}{h}\int_{-\infty}^{\infty} dE\, P(E) f(\varepsilon_i + E),$$
$$\Gamma_{i-}(\varepsilon_i) = N\frac{\Gamma_i}{h}\int_{-\infty}^{\infty} dE\, P(-E)[1 - f(\varepsilon_i + E)]. \tag{D1}$$

Here Γ_i is the tunnel coupling strength, ε_i is the QD energy level position with respect to the reservoir Fermi level, $f(E)$ is the Fermi function defining the electron occupation distribution in the reservoir, and the additional prefactor N for tunneling out arises from the degeneracy of the considered QD energy level [16,51], as above. For our system, we have $N = 2$ because there are two electrons to choose from to tunnel out and only one vacant state to tunnel into the QD.

The $P(E)$ function is set by the environment. In our case, the resonator forms a single-photon mode at frequency ω_r as the environment [34,54]. For the characteristic impedance $Z_0 = 53\Omega$ of our resonator, we have $z = \pi Z_0 G_0 \ll 1$, where $G_0 = e^2/h$ is the conductance quantum. For the coherent drive used in the experiment with low enough input power and at low temperature $kT \ll \hbar\omega_r$, the resonator is in a coherent state with a small photon number $\langle n\rangle \ll 1/z$. In this limit, the $P(E)$ function reads [34]

$$P(E) = [1 - z\nu^2(2\langle n\rangle + 1)]\delta(E) + z\nu^2\langle n\rangle\,\delta(E + \hbar\omega) + z\nu^2(\langle n\rangle + 1)\delta(E - \hbar\omega), \tag{D2}$$

where ν is the fraction of the resonator voltage that appears across the tunnel barrier where the tunneling takes place [55]. We assume that the junction capacitances of the quantum dot are equal. In addition, the gate capacitance is much smaller than the junction capacitances in the studied devices. Under these conditions, the resonator voltage is divided evenly over the two tunnel barriers, $\nu = 1/2$, and the $P(E)$ function is the same for the two tunnel junctions.

The three terms in Eq. (D2) correspond to (1) no interactions with the photons, (2) absorption of a photon, and (3) emission of a photon with probabilities $P_0 = 1 - z\nu^2(2\langle n\rangle + 1)$, $P_{-1} = z\nu^2\langle n\rangle$, and $P_{+1} = z\nu^2(\langle n\rangle + 1)$ respectively. Interestingly, the photon absorption or emission probability is solely set by the impedance z, coupling ν, and photon number $\langle n\rangle$ of the microwave resonator and does not depend on the tunnel coupling Γ_i. The absorption and emission rates, however, depend on Γ_i via Eq. (D1). Note also that Eq. (D2) contains only single-photon absorption and emission processes. Multiphoton processes are suppressed in the low drive limit $\langle n\rangle \ll 1/(z\nu^2)$, in line with the experiments in Ref. [48].

APPENDIX E: TUNNELING RATES AND ELECTRICAL CONDUCTION

With Eqs. (D1) and (D2), we obtain the tunneling rates

$$\begin{aligned}\Gamma_{i+}(\varepsilon_i) &= \frac{\Gamma_i}{h}[P_0 f(\varepsilon_i) + P_{-1} f(\varepsilon_i - \hbar\omega) + P_{+1} f(\varepsilon_i + \hbar\omega)],\\ \Gamma_{i-}(\varepsilon_i) &= N\frac{\Gamma_i}{h}\{P_0[1 - f(\varepsilon_i)] + P_{-1}[1 - f(\varepsilon_i + \hbar\omega)]\\ &\quad + P_{+1}[1 - f(\varepsilon_i - \hbar\omega)]\} = N\Gamma_{i+}(-\varepsilon_i).\end{aligned} \tag{E1}$$

The energy differences across the two junctions are $\varepsilon_\mathrm{L} = \varepsilon_d + \alpha V_G - eV_\mathrm{b}/2$ and $\varepsilon_\mathrm{R} = \varepsilon_d + \alpha V_G + eV_\mathrm{b}/2$, where α is the gate lever arm, V_g is the voltage applied to a gate electrode, and V_b is the bias voltage between the source and drain. Here we have again assumed that the junction capacitances are equal and the gate capacitance is small compared to the junction capacitances which divide the bias voltage V_b evenly over the junctions.

Next, we determine the electrical conductance G by setting a rate equation to describe the probability p of having an excess electron in the QD and the probability $(1-p)$ of not having the excess electron. This rate equation reads

$$\frac{dp}{dt} = -\Gamma_- p + \Gamma_+ (1-p), \tag{E2}$$

where $\Gamma_- = \Gamma_{\mathrm{L}-}(\varepsilon_\mathrm{L}) + \Gamma_{\mathrm{R}-}(\varepsilon_\mathrm{R})$ is the sum of the rates for the electron to tunnel out and $\Gamma_+ = \Gamma_{\mathrm{L}+}(\varepsilon_\mathrm{L}) + \Gamma_{\mathrm{R}+}(\varepsilon_\mathrm{R})$ is the sum of the rates to tunnel in. The steady-state solution, $dp/dt = 0$, is

$$p = \frac{\Gamma_+}{\Gamma_+ + \Gamma_-}. \tag{E3}$$

The electrical current I through the QD is given by

$$\begin{aligned}I &= e[\Gamma_{\mathrm{L}+}(\varepsilon_\mathrm{L})(1-p) - \Gamma_{\mathrm{L}-}(\varepsilon_\mathrm{L})\,p]\\ &= e\frac{\Gamma_{\mathrm{L}+}(\varepsilon_\mathrm{L})\Gamma_{\mathrm{R}-}(\varepsilon_\mathrm{R}) - \Gamma_{\mathrm{L}-}(\varepsilon_\mathrm{L})\Gamma_{\mathrm{R}+}(\varepsilon_\mathrm{R})}{\Gamma_{\mathrm{L}+}(\varepsilon_\mathrm{L}) + \Gamma_{\mathrm{R}+}(\varepsilon_\mathrm{R}) + \Gamma_{\mathrm{L}-}(\varepsilon_\mathrm{L}) + \Gamma_{\mathrm{R}-}(\varepsilon_\mathrm{R})}.\end{aligned} \tag{E4}$$

Finally, the differential conductance is obtained as

$$G = \frac{dI}{dV_\mathrm{SD}}. \tag{E5}$$

For small bias voltage, $eV_\mathrm{SD} \ll kT$, and low photon absorption and emission probabilities, $P_{-1}, P_{+1} \ll P_0$, we obtain

$$\begin{aligned}G &= \frac{e^2}{hkT}\,\frac{\Gamma_\mathrm{L}\Gamma_\mathrm{R}}{\Gamma_\mathrm{L}+\Gamma_\mathrm{R}}\\ &\quad\times \frac{1}{1 + \frac{1}{N} + \frac{2}{\sqrt{N}}\cosh\left[(\varepsilon_d + \alpha V_G)/kT + \frac{1}{2}\ln N\right]},\end{aligned} \tag{E6}$$

which is the zero bias conductance G for a QD with degeneracy N and matches Eq. (C12). Compared to the standard nondegenerate result with $N = 1$, the degeneracy $N \neq 1$ keeps the line shape the same but displaces the peak position by $(kT\ln N)/2$ in energy and increases the maximum value by a factor of $4/(1+1/\sqrt{N})^2$. For $N = 2$, these are both small effects: $(kT\ln N)/2 \approx 0.35\,kT$ and $4/(1+1/\sqrt{N})^2 \approx 1.37$. With photon absorption accounted for, two side peaks appear in G. These are separated by $\hbar\omega$ in energy from the main conduction peak. The size of these peaks are P_{-1}/P_0 relative to the main peak and can therefore be neglected for our devices with $P_{-1} \ll P_0$.

APPENDIX F: PHOTON ABSORPTION AND EMISSION RATES

Above, we determined the low-frequency electrical conductance G. By collecting the photon absorption terms from Eq. (E1), we obtain the photon absorption rate

$$\begin{aligned}\Gamma_-^\mathrm{photon} &= P_{-1}\{[\Gamma_\mathrm{L}\, f(\varepsilon_\mathrm{L} - \hbar\omega) + \Gamma_\mathrm{R}\, f(\varepsilon_\mathrm{R} - \hbar\omega)](1-p)\\ &\quad + N[\Gamma_\mathrm{L}\, f(-\varepsilon_\mathrm{L} - \hbar\omega) + \Gamma_\mathrm{R}\, f(-\varepsilon_\mathrm{R} - \hbar\omega)]p\}/h,\end{aligned} \tag{F1}$$

where we have summed the absorption terms with the corresponding weights of $(1-p)$ and p of the probability to be in the right starting state of the QD. The absorption rate per photon corresponds to a resonator loss term κ_QD, which is thus

$$\begin{aligned}\kappa_\mathrm{QD} &= \frac{\Gamma_-^\mathrm{photon}}{\langle n\rangle}\\ &= \nu^2 z\{[\Gamma_\mathrm{L}\, f(\varepsilon_\mathrm{L} - \hbar\omega) + \Gamma_\mathrm{R}\, f(\varepsilon_\mathrm{R} - \hbar\omega)](1-p)\\ &\quad + N[\Gamma_\mathrm{L}\, f(-\varepsilon_\mathrm{L} - \hbar\omega) + \Gamma_\mathrm{R}\, f(-\varepsilon_\mathrm{R} - \hbar\omega)]p\}/h.\end{aligned} \tag{F2}$$

For zero bias voltage, $V_\mathrm{SD} = 0$, at low temperature, $kT \ll \hbar\omega$, and for a small photon number $\langle n\rangle$, we have $\varepsilon_\mathrm{L} = \varepsilon_\mathrm{R}$, and the photon absorption takes place in two distinct regimes. The first one has $-\hbar\omega < \varepsilon_i < 0$. Here we have $p = 1$; that is, the quantum dot is occupied essentially at all times, and $f(-\varepsilon_i - \hbar\omega) = 1$. With this, Eq. (F2) yields

$$\kappa_\mathrm{QD} = z\nu^2(\Gamma_\mathrm{L} + \Gamma_\mathrm{R})N/h. \tag{F3}$$

The other regime takes place for $0 < \varepsilon_i < \hbar\omega$. In this case we have the QD essentially always unoccupied, i.e., $p = 0$, while the energy ε_i is still low enough that $f(\varepsilon_i - \hbar\omega) = 1$. Now we have

$$\kappa_\mathrm{QD} = z\nu^2(\Gamma_\mathrm{L} + \Gamma_\mathrm{R})/h, \tag{F4}$$

which is the same as above but smaller by the degeneracy factor N. The sum $(\Gamma_\mathrm{L} + \Gamma_\mathrm{R})$ reflects the fact that with no bias voltage applied, the two junctions are effectively in parallel. The dashed lines in Fig. 2(d) in the main text are the results of Eqs. (F3) and (F4) and show that the measured response follows these values. The fitted solid curve in Fig. 2(d), based on Appendix C, is essentially the same as the result of Eq. (F2). This demonstrates that the two sequential tunneling models yield identical results in this regime. For a stronger coupling via larger impedance Z_0, deviances are expected: In the absence of the drive, the calculation in Appendix C still predicts no changes to the standard DC transport result, while the $P(E)$ theory has a strong spontaneous emission process and thus a suppressed probability P_0 for the DC transport known as the dynamical Coulomb blockade [56].

[1] B. E. Kane, Nature (London) **393**, 133 (1998).
[2] D. Loss and D. P. DiVincenzo, Phys. Rev. A **57**, 120 (1998).
[3] L. M. K. Vandersypen, H. Bluhm, J. S. Clarke, A. S. Dzurak, R. Ishihara, A. Morello, D. J. Reilly, L. R. Schreiber, and M. Veldhorst, npj Quantum Inf. **3**, 34 (2017).
[4] R. Hanson, L. P. Kouwenhoven, J. R. Petta, S. Tarucha, and L. M. K. Vandersypen, Rev. Mod. Phys. **79**, 1217 (2007).
[5] M. W. Keller, A. L. Eichenberger, J. M. Martinis, and N. M. Zimmerman, Science **285**, 1706 (1999).
[6] J. P. Pekola, O.-P. Saira, V. F. Maisi, A. Kemppinen, M. Möttönen, Y. A. Pashkin, and D. V. Averin, Rev. Mod. Phys. **85**, 1421 (2013).
[7] D. J. van Woerkom, A. Geresdi, and L. P. Kouwenhoven, Nat. Phys. **11**, 547 (2015).
[8] E. T. Mannila, P. Samuelsson, S. Simbierowicz, J. T. Peltonen, V. Vesterinen, L. Grönberg, J. Hassel, V. F. Maisi, and J. P. Pekola, Nat. Phys. **18**, 145 (2022).
[9] A. Ranni, F. Brange, E. T. Mannila, C. Flindt, and V. F. Maisi, Nat. Commun. **12**, 6358 (2021).
[10] S. Gustavsson, M. Studer, R. Leturcq, T. Ihn, K. Ensslin, D. C. Driscoll, and A. C. Gossard, Phys. Rev. Lett. **99**, 206804 (2007).
[11] A. Ghirri, S. Cornia, and M. Affronte, Sensors **20**, 4010 (2020).
[12] W. Khan, P. P. Potts, S. Lehmann, C. Thelander, K. A. Dick, P. Samuelsson, and V. F. Maisi, Nat. Commun. **12**, 5130 (2021).
[13] S. Cornia, V. Demontis, V. Zannier, L. Sorba, A. Ghirri, F. Rossella, and M. Affronte, Adv. Funct. Mater. **33**, 2212517 (2023).
[14] J. V. Koski, V. F. Maisi, J. P. Pekola, and D. V. Averin, Proc. Natl. Acad. Sci. USA **111**, 13786 (2014).
[15] J. V. Koski, V. F. Maisi, T. Sagawa, and J. P. Pekola, Phys. Rev. Lett. **113**, 030601 (2014).
[16] D. Barker, M. Scandi, S. Lehmann, C. Thelander, K. A. Dick, M. Perarnau-Llobet, and V. F. Maisi, Phys. Rev. Lett. **128**, 040602 (2022).
[17] R. Garreis, J. D. Gerber, V. Stará, C. Tong, C. Gold, M. Röösli, K. Watanabe, T. Taniguchi, K. Ensslin, T. Ihn, and A. Kurzmann, Phys. Rev. Res. **5**, 013042 (2023).
[18] B. Küng, C. Rössler, M. Beck, M. Marthaler, D. S. Golubev, Y. Utsumi, T. Ihn, and K. Ensslin, Phys. Rev. X **2**, 011001 (2012).
[19] G. Manzano, D. Subero, O. Maillet, R. Fazio, J. P. Pekola, and E. Roldán, Phys. Rev. Lett. **126**, 080603 (2021).
[20] T. Ihn, Quantum dots, *Semiconductor Nanostructures: Quantum States and Electronic Transport* (Oxford Academic, Oxford, 2009).
[21] J. H. Davies, Tunnelling transport, *The Physics of Low-Dimensional Semiconductors: An Introduction* (Cambridge University Press, Cambridge, 1997), pp. 150–205.
[22] P. Lafarge, P. Joyez, D. Esteve, C. Urbina, and M. H. Devoret, Phys. Rev. Lett. **70**, 994 (1993).
[23] R. J. Schoelkopf, P. Wahlgren, A. A. Kozhevnikov, P. Delsing, and D. E. Prober, Science **280**, 1238 (1998).
[24] E. J. Connors, J. J. Nelson, and J. M. Nichol, Phys. Rev. Appl. **13**, 024019 (2020).
[25] Y.-Y. Liu, S. G. J. Philips, L. A. Orona, N. Samkharadze, T. McJunkin, E. R. MacQuarrie, M. A. Eriksson, L. M. K. Vandersypen, and A. Yacoby, Phys. Rev. Appl. **16**, 014057 (2021).
[26] Y. Li, S.-X. Li, F. Gao, H.-O. Li, G. Xu, K. Wang, H. Liu, G. Cao, M. Xiao, T. Wang, J.-J. Zhang, and G.-P. Guo, J. Appl. Phys. **123**, 174305 (2018).
[27] X. Mi, J. V. Cady, D. M. Zajac, P. W. Deelman, and J. R. Petta, Science **355**, 156 (2017).
[28] A. Stockklauser, P. Scarlino, J. V. Koski, S. Gasparinetti, C. K. Andersen, C. Reichl, W. Wegscheider, T. Ihn, K. Ensslin, and A. Wallraff, Phys. Rev. X **7**, 011030 (2017).
[29] M.-C. Harabula, T. Hasler, G. Fülöp, M. Jung, V. Ranjan, and C. Schönenberger, Phys. Rev. Appl. **8**, 054006 (2017).
[30] D. de Jong, C. G. Prosko, D. M. A. Waardenburg, L. Han, F. K. Malinowski, P. Krogstrup, L. P. Kouwenhoven, J. V. Koski, and W. Pfaff, Phys. Rev. Appl. **16**, 014007 (2021).
[31] T. Frey, P. J. Leek, M. Beck, J. Faist, A. Wallraff, K. Ensslin, T. Ihn, and M. Büttiker, Phys. Rev. B **86**, 115303 (2012).
[32] C. Bruder and H. Schoeller, Phys. Rev. Lett. **72**, 1076 (1994).
[33] G.-L. Ingold and Y. V. Nazarov, Charge tunneling rates in ultrasmall junctions, in *Single Charge Tunneling: Coulomb Blockade Phenomena in Nanostructures*, edited by H. Grabert and M. H. Devoret (Springer, Boston, 1992), pp. 21–107.
[34] J.-R. Souquet, M. J. Woolley, J. Gabelli, P. Simon, and A. A. Clerk, Nat. Commun. **5**, 5562 (2014).
[35] M. Göppl, A. Fragner, M. Baur, R. Bianchetti, S. Filipp, J. M. Fink, P. J. Leek, G. Puebla, L. Steffen, and A. Wallraff, J. Appl. Phys. **104**, 113904 (2008).
[36] K. A. Dick, J. Bolinsson, M. E. Messing, S. Lehmann, J. Johansson, and P. Caroff, J. Vac. Sci. Technol. B **29**, 04D103 (2011).
[37] I.-J. Chen, S. Lehmann, M. Nilsson, P. Kivisaari, H. Linke, K. A. Dick, and C. Thelander, Nano Lett. **17**, 902 (2017).
[38] M. Nilsson, L. Namazi, S. Lehmann, M. Leijnse, K. A. Dick, and C. Thelander, Phys. Rev. B **93**, 195422 (2016).
[39] D. Barker, S. Lehmann, L. Namazi, M. Nilsson, C. Thelander, K. A. Dick, and V. F. Maisi, Appl. Phys. Lett. **114**, 183502 (2019).
[40] J. Stehlik, Y.-Y. Liu, C. M. Quintana, C. Eichler, T. R. Hartke, and J. R. Petta, Phys. Rev. Appl. **4**, 014018 (2015).
[41] A. Prêtre, H. Thomas, and M. Büttiker, Phys. Rev. B **54**, 8130 (1996).
[42] P. Simonet, C. Rössler, T. Krähenmann, A. Varlet, T. Ihn, K. Ensslin, C. Reichl, and W. Wegscheider, Appl. Phys. Lett. **107**, 023105 (2015).
[43] L. P. Kouwenhoven, S. Jauhar, J. Orenstein, P. L. McEuen, Y. Nagamune, J. Motohisa, and H. Sakaki, Phys. Rev. Lett. **73**, 3443 (1994).
[44] M. Josefsson, A. Svilans, A. M. Burke, E. A. Hoffmann, S. Fahlvik, C. Thelander, M. Leijnse, and H. Linke, Nat. Nanotechnol. **13**, 920 (2018).
[45] S. Cornia, F. Rossella, V. Demontis, V. Zannier, F. Beltram, L. Sorba, M. Affronte, and A. Ghirri, Sci. Rep. **9**, 19523 (2019).
[46] T. Frey, P. J. Leek, M. Beck, K. Ensslin, A. Wallraff, and T. Ihn, Appl. Phys. Lett. **98**, 262105 (2011).
[47] J. M. Sage, V. Bolkhovsky, W. D. Oliver, B. Turek, and P. B. Welander, J. Appl. Phys. **109**, 063915 (2011).
[48] S. Haldar, H. Havir, W. Khan, S. Lehmann, C. Thelander, K. A. Dick, and V. F. Maisi, Phys. Rev. Lett. **130**, 087003 (2023).

[49] M. Ridley, N. W. Talarico, D. Karlsson, N. L. Gullo, and R. Tuovinen, J. Phys. A **55**, 273001 (2022).

[50] S. J. Chorley, J. Wabnig, Z. V. Penfold-Fitch, K. D. Petersson, J. Frake, C. G. Smith, and M. R. Buitelaar, Phys. Rev. Lett. **108**, 036802 (2012).

[51] A. Hofmann, V. F. Maisi, C. Gold, T. Krähenmann, C. Rössler, J. Basset, P. Märki, C. Reichl, W. Wegscheider, K. Ensslin, and T. Ihn, Phys. Rev. Lett. **117**, 206803 (2016).

[52] T. Ihn, *Semiconductor Nanostructures* (Oxford University Press, New York, 2010).

[53] V. F. Maisi, Ph.D. thesis, Aalto University, 2014.

[54] S. M. Girvin, Circuit QED: Superconducting qubits coupled to microwave photons, in *Quantum Machines: Measurement and Control of Engineered Quantum Systems*, Lecture Notes of the Les Houches Summer School Vol. 96 (Oxford University Press, Oxford, 2014), pp. 113–256.

[55] L. Childress, A. S. Sørensen, and M. D. Lukin, Phys. Rev. A **69**, 042302 (2004).

[56] C. Altimiras, O. Parlavecchio, P. Joyez, D. Vion, P. Roche, D. Esteve, and F. Portier, Phys. Rev. Lett. **112**, 236803 (2014).